Optical design and imaging performance testing of a 9.6-mm diameter femtosecond laser microsurgery probe

Christopher L. Hoy,[1] Onur Ferhanoğlu,[1] Murat Yildirim,[1] Wibool Piyawattanametha,[2] Hyejun Ra,[2] Olav Solgaard,[2] and Adela Ben-Yakar[1,*]

[1]*Department of Mechanical Engineering, The University of Texas at Austin, Austin, Texas 78712, USA*
[2]*Department of Electrical Engineering, Stanford University, Stanford, California 945305, USA*
**ben-yakar@mail.utexas.edu*

Abstract: We present the optical design of a 9.6-mm diameter fiber-coupled probe for combined femtosecond laser microsurgery and nonlinear optical imaging. Towards enabling clinical use, we successfully reduced the dimensions of our earlier 18-mm microsurgery probe by half, while improving optical performance. We use analytical and computational models to optimize the miniaturized lens system for off-axis scanning aberrations. The optimization reveals that the optical system can be aberration-corrected using simple aspheric relay lenses to achieve diffraction-limited imaging resolution over a large field of view. Before moving forward with custom lenses, we have constructed the 9.6-mm probe using off-the-shelf spherical relay lenses and a 0.55 NA aspheric objective lens. In addition to reducing the diameter by nearly 50% and the total volume by 5 times, we also demonstrate improved lateral and axial resolutions of 1.27 µm and 13.5 µm, respectively, compared to 1.64 µm and 16.4 µm in our previous work. Using this probe, we can successfully image various tissue samples, such as rat tail tendon that required 2-3 × lower laser power than the current state-of-the-art. With further development, image-guided, femtosecond laser microsurgical probes such as this one can enable physicians to achieve the highest level of surgical precision anywhere inside the body.

OCIS codes: (170.2150) Endoscopic imaging; (220.4830) Systems design; (180.4315) Nonlinear microscopy.

References and links

1. A. Vogel, J. Noack, G. Hüttman, and G. Paltauf, "Mechanisms of femtosecond laser nanosurgery of cells and tissues," Appl. Phys. B **81**(8), 1015–1047 (2005).
2. H. K. Soong, and J. B. Malta, "Femtosecond lasers in ophthalmology," Am. J. Ophthalmol. **147**(2), 189–197, e2 (2009).
3. A. V. Rode, E. G. Gamaly, B. Luther-Davies, B. T. Taylor, J. Dawes, A. Chan, R. M. Lowe, and P. Hannaford, "Subpicosecond laser ablation of dental enamel," J. Appl. Phys. **92**(4), 2153–2158 (2002).
4. M. H. Niemz, A. Kasenbacher, M. Strassl, A. Bäcker, A. Beyertt, D. Nickel, and A. Giesen, "Tooth ablation using a CPA-free thin disk femtosecond laser system," Appl. Phys. B **79**, 269–271 (2004).
5. W. B. Armstrong, J. A. Neev, L. B. Da Silva, A. M. Rubenchik, and B. C. Stuart, "Ultrashort pulse laser ossicular ablation and stapedotomy in cadaveric bone," Lasers Surg. Med. **30**(3), 216–220 (2002).
6. J. Ilgner, M. Wehner, J. Lorenzen, M. Bovi, and M. Westhofen, "Morphological effects of nanosecond- and femtosecond-pulsed laser ablation on human middle ear ossicles," J. Biomed. Opt. **11**(1), 014004 (2006).
7. R. G. McCaughey, H. Sun, V. S. Rothholtz, T. Juhasz, and B. J. F. Wong, "Femtosecond laser ablation of the stapes," J. Biomed. Opt. **14**(2), 024040–024046 (2009).
8. H. Wisweh, U. Merkel, A. K. Huller, K. Lurben, and H. Lubatschowski, "Optical coherence tomography monitoring of vocal fold femtosecond laser microsurgery " in *Therapeutic Laser Applications and Laser-Tissue Interaction III*, A. Vogel, ed. (2007), p. 63207.
9. C. L. Hoy, W. N. Everett, J. Kobler, and A. Ben-Yakar, "Toward endoscopic ultrafast laser microsurgery of vocal folds," Proc. SPIE **7548**, 754831 (2010).

#141745 - $15.00 USD Received 26 Jan 2011; revised 23 Feb 2011; accepted 18 Mar 2011; published 13 May 2011

10. C. L. Hoy, N. J. Durr, P. Chen, W. Piyawattanametha, H. Ra, O. Solgaard, and A. Ben-Yakar, "Miniaturized probe for femtosecond laser microsurgery and two-photon imaging," Opt. Express **16**(13), 9996–10005 (2008).
11. N. J. Durr, T. Larson, D. K. Smith, B. A. Korgel, K. Sokolov, and A. Ben-Yakar, "Two-photon luminescence imaging of cancer cells using molecularly targeted gold nanorods," Nano Lett. **7**(4), 941–945 (2007).
12. H. Ürey, "Spot size, depth-of-focus, and diffraction ring intensity formulas for truncated Gaussian beams," Appl. Opt. **43**(3), 620–625 (2004).
13. R. Le Harzic, M. Weinigel, I. Riemann, K. König, and B. Messerschmidt, "Nonlinear optical endoscope based on a compact two axes piezo scanner and a miniature objective lens," Opt. Express **16**(25), 20588–20596 (2008).
14. K. Carlsson, "The influence of specimen refractive index, detector signal integration, and non-uniform scan speed on the imaging properties in confocal microscopy," J. Microsc. **163**, 167–178 (1991).
15. T. D. Visser, J. L. Oud, and G. J. Brakenhoff, "Refractive index and axial distance measurements in 3-D microscopy," Optik (Stuttg.) **90**, 17–19 (1992).
16. D. Lee, and O. Solgaard, "Two-axis gimbaled microscanner in double SOI layers actuated by self-aligned vertical electrostatic combdrive," in *Proceedings of the Solid-State Sensors, Actuators and Microsystems Workshop, Hilton Head Island*, (Hilton Head Island, South Carolina, 2004), pp. 352–355.
17. G. F. Marshall, *Handbook of optical and laser scanning* (Marcel Dekker, 2004).
18. R. R. Shannon, *The Art and Science of Optical Design* (Cambridge University Press, 1997).
19. E. Salomatina, B. Jiang, J. Novak, and A. N. Yaroslavsky, "Optical properties of normal and cancerous human skin in the visible and near-infrared spectral range," J. Biomed. Opt. **11**(6), 064026 (2006).
20. R. Drezek, K. Sokolov, U. Utzinger, I. Boiko, A. Malpica, M. Follen, and R. Richards-Kortum, "Understanding the contributions of NADH and collagen to cervical tissue fluorescence spectra: modeling, measurements, and implications," J. Biomed. Opt. **6**(4), 385–396 (2001).
21. C. L. Hoy, N. J. Durr, and A. Ben-Yakar, "Fast-updating and non-repeating Lissajous image reconstruction method for capturing increased dynamic information," Appl. Opt. in press.
22. W. Göbel, J. N. D. Kerr, A. Nimmerjahn, and F. Helmchen, "Miniaturized two-photon microscope based on a flexible coherent fiber bundle and a gradient-index lens objective," Opt. Lett. **29**(21), 2521–2523 (2004).
23. W. Piyawattanametha, E. D. Cocker, R. P. J. Barretto, J. C. Jung, B. A. Flusberg, H. Ra, O. Solgaard, and M. J. Schnitzer, "A portable two-photon fluorescence microendoscope based on a two-dimensional scanning mirror," in *IEEE/LEOS International Conference on Optical MEMS and Nanophotonics*, (Hualien, Taiwan, 2007).
24. G. Liu, T. Xie, I. V. Tomov, J. Su, L. Yu, J. Zhang, B. J. Tromberg, and Z. Chen, "Rotational multiphoton endoscopy with a 1 microm fiber laser system," Opt. Lett. **34**(15), 2249–2251 (2009).
25. Y. Wu, Y. Leng, J. Xi, and X. Li, "Scanning all-fiber-optic endomicroscopy system for 3D nonlinear optical imaging of biological tissues," Opt. Express **17**(10), 7907–7915 (2009).
26. G. Liu, K. Kieu, F. W. Wise, and Z. Chen, "Multiphoton microscopy system with a compact fiber-based femtosecond-pulse laser and handheld probe," J Biophotonics **4**(1-2), 34–39 (2011).
27. C. L. Hoy, N. Durr, P. Chen, D. K. Smith, T. Larson, W. Piyawattanametha, H. Ra, B. Korgel, K. Sokolov, O. Solgaard, and A. Ben-Yakar, "Two-Photon Luminescence Imaging Using a MEMS-Based Miniaturized Probe," in *Conference on Lasers and Electro-Optics (CLEO)*, (Optical Society of America, 2008), paper CThG5.
28. L. Fu, A. Jain, C. Cranfield, H. Xie, and M. Gu, "Three-dimensional nonlinear optical endoscopy," J. Biomed. Opt. **12**(4), 040501 (2007).

1. Introduction

Ablation with femtosecond laser pulses provides unrivaled microsurgical precision in bulk scattering tissue, with minimal thermal or mechanical side effects [1]. As a result, femtosecond laser microsurgery has gained increasing clinical acceptance in a number of ophthalmic applications [2]. Many other clinical applications have been identified in fields such as dentistry [3,4], otology [5–7], and laryngology [8,9], for example. Unlike ophthalmic applications, these applications require or would benefit from fiber optic delivery of amplified femtosecond laser pulses to the surgical site through a flexible, miniaturized probe. The lack of fiber delivery and precise guidance present hurdles for developing such applications.

Towards meeting this need, we have recently developed a fiber-coupled and miniaturized femtosecond laser microsurgery probe [10]. In addition to delivering amplified pulses for microsurgery, this system also delivered unamplified pulses at a high repetition rate for nonlinear imaging via two-photon fluorescence. By using the same optical system for both microsurgery and imaging, the probe could provide microscopic visual guidance with the same operating field and resolution as the surgery. With this first probe we successfully demonstrated image-guided cellular ablation in carcinoma cell cultures.

Towards clinical development of this image-guided surgery probe, we have sought to further miniaturize the probe beyond its 18-mm diameter, to improve packaging integration to flexibly decouple the probe from the optical bench, and to improve its imaging performance. This paper focuses on the optical design of a new microsurgery and nonlinear imaging probe with greatly reduced outer diameter and improved imaging capabilities.

#141745 - $15.00 USD Received 26 Jan 2011; revised 23 Feb 2011; accepted 18 Mar 2011; published 13 May 2011

The paper is organized into three sections. First, we experimentally characterize several commercial miniature objective lenses, including both aspheric and gradient index (GRIN) lenses. Second, we use both analytical design equations and ZEMAX optical simulations to develop an aberration-corrected miniature relay lens system for use with the commercial objective lenses. Finally, we present the realization of our design in a new 9.6-mm diameter probe using an inexpensive spherical relay lens pair and provide characterization of its performance for nonlinear imaging of various tissue samples.

2. Description and selection of critical components

The optical system of our image-guided surgery probes is tailored to enable both nonlinear optical imaging and microsurgery with amplified femtosecond laser pulses. While maintaining the successful optical layout of our earlier 18-mm probe, here we wish to optimize its imaging performance and reduce the encircling diameter. The encircling diameter is the smallest diameter housing that can be used to deliver the entire probe. We successfully reduced the encircling diameter of the new probe to 9.6 mm by reducing the size of the each component, as will be discussed throughout the paper (Fig. 1a). This section will focus on the selection of the critical components for the revised probe and particular attention will be given to the characterization of miniature objective lenses.

2.1 Optical layout

The general optical layout of our probes, shown in Fig. 1b, consists of 5 critical components: 1) an air-core photonic bandgap fiber (PBF; Air-6-800, Crystal Fibre) with GRIN collimating lens, 2) a microelectromechanical system (MEMS) scanning mirror, 3) a pair of relay lenses to image the scanning mirror to the objective lens, 4) an objective lens, and 5) a separate large area optical fiber with a dichroic mirror for fluorescence emission collection.

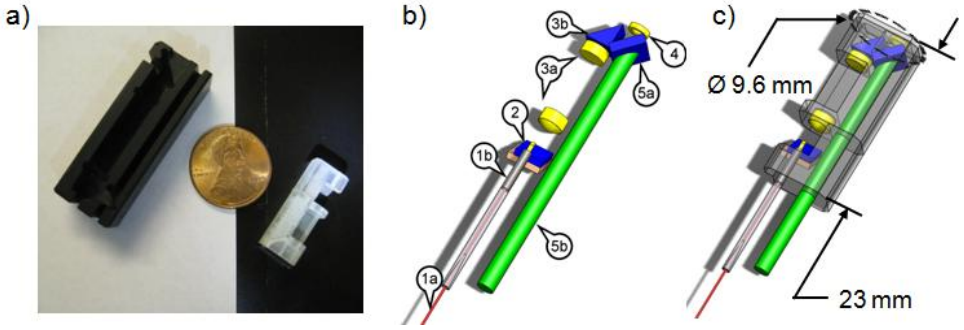

Fig. 1. Optical system of the new 9.6-mm probe. a) A photograph of the 9.6-mm probe housing (right) next to the housing of the 18-mm probe (left) showing the reduction in packaged probe size. A US penny is shown for scale. b) The components include: (1a) three meters of PBF; (1b) the fiber collimation assembly; (2) a two-axis MEMS scanning mirror; (3a) a pair of spherical relay lenses with 2.32 × magnification; (3b) a right angle TIR prism; (4) a 0.55 NA aspheric objective lens; (5a) a dichroic mirror; and (5b) one meter of 2 mm core plastic optical fiber. c) The packaged endoscope is shown transparently overlaid with the optical system.

In this layout, the PBF allows for flexible delivery of the high intensity pulses required for microsurgery without inducing self-phase modulation along the fiber or damaging the fiber. The MEMS scanning mirror enables Lissajous scanning of the imaging laser beam to provide image-guidance for microsurgery. The relay lens pair provides one of the most important features of this layout that is to achieve a uniformly illuminated field of view (FOV). By using a pair of relay lenses, a dichroic mirror and dedicated fluorescence emission collection fiber can be placed close to the objective lens for improved collection of emitted photons. In addition, the relay lenses provide magnification of the incoming laser beam, which provides flexibility in determining resolution and FOV trade-offs. The use of conventional lenses rather than a multipitch GRIN relay lens avoids creating intermediate foci and long propagation

#141745 - $15.00 USD Received 26 Jan 2011; revised 23 Feb 2011; accepted 18 Mar 2011; published 13 May 2011

lengths in glass, which can lead to unwanted self-phase modulation and material damage when using amplified pulses for microsurgery.

2.2 Miniature objective lens

The 18-mm probe utilized a GRIN objective lens (LGI830-1, Newport) with 0.46 numerical aperture (NA) manufactured by Nippon Sheet Glass (NSG). With this lens, the two-photon fluorescence lateral and axial resolutions were measured to be 1.64 μm and 16.4 μm, respectively [10]. This resolution is not diffraction-limited and exhibits significant aberrations. Since this aberration has been widely attributed to spherical aberration in GRIN lenses, we investigated the focusing capabilities of a range of off-the-shelf miniature lenses.

We identified four commercially available lenses with diameters and NA suitable for use as a miniature objective lens at near infrared (NIR) wavelengths. The first lens (GT-LFRL-180-023-50, GRINTECH) is another GRIN lens with similar specifications to the previous objective lens. The remaining three lenses (352150, 350140, and 372840; Lightpath Technologies) are aspheric singlet lenses with NAs ranging from 0.50 to 0.80. Table 1 provides a summary of their relevant specifications.

Table 1. Summary of Commercially Available Lenses Considered for Use as the Miniature Objective Lens

	NA	OD [mm]	CA [mm]	WD [mm]	FL [mm]	λ_d [nm]
Newport (NSG) LGI830-1[1]	0.46	1.8	1.26	0.21	1.38	830
GRINTECH GT-LFRL-180-023-50	0.49	1.8	1.62	0.23	1.78	810
Lightpath 352150	0.5	3.0	2.00	1.09	2.00	780
Lightpath 352140	0.55	2.4	1.60	0.88	1.45	780
Lightpath 370840	0.80	3.0	1.20	0.2	0.75	1550

[1]The objective lens used in the original 18-mm probe is provided here for comparison. (NA: numerical aperture; OD: outer diameter; CA: clear aperture; WD: working distance; FL: focal length; λ_d: design wavelength.)

We tested the performance of each lens in a bench-top two-photon microscope, described in Fig. 2 [11], where we fabricated an adapter to mount each lens in place of the full-size objective lens. The two-photon PSF of each lens was then measured by imaging 100 nm fluorescent beads suspended in a 4% agar gel (0.002% solids). To model imaging conditions in the probe, we tuned a Ti:sapphire oscillator (80 MHz repetition rate Mai Tai, Spectra Physics) to 753 nm, near the minimum dispersion wavelength of the air-core PBF. Since the clear aperture dimensions of the lenses vary, the beam diameter at the back aperture was adjusted to approximately 4 mm ($1/e^2$). This large beam size ensured the truncation ratio for each lens exceeded 2.0 and therefore each lens could be said to be equally overfilled [12].

The optimum beam quality in the endoscope will be determined by the beam emerging from the PBF and the collimating lens. Since GRIN lenses remain the optimum choice for achieving the smallest outer diameter of the fiber collimating assembly, we also repeated the PSF measurements using a beam delivered through one meter of the PBF and collimated by the GRINTECH GRIN lens. The beam was again expanded to 4 mm to be consistent with the measurements made without the fiber.

#141745 - $15.00 USD Received 26 Jan 2011; revised 23 Feb 2011; accepted 18 Mar 2011; published 13 May 2011

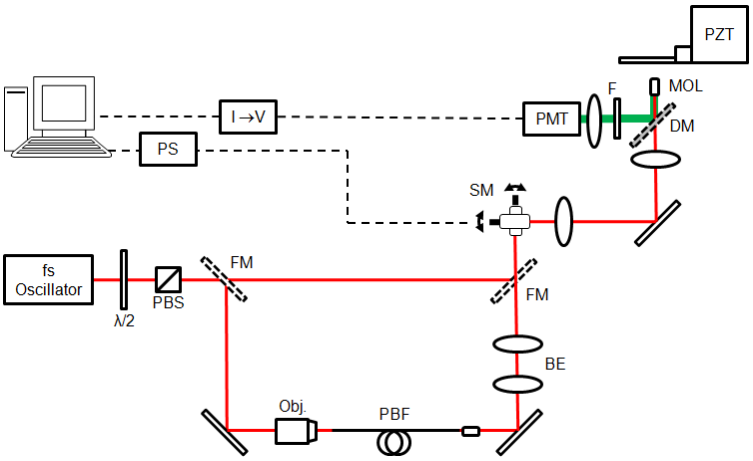

Fig. 2. Experimental setup for measuring the PSF of miniature objective lenses. The system consists of a home-built inverted two-photon microscope in which a miniature lens is used in place of a traditional objective lens. An optional beam path can deliver the laser pulses through one meter of PBF. Care was taken to maintain a beam diameter at the miniature objective lens back aperture of approximately 4 mm ($1/e^2$) for both optical paths. λ/2: half wave plate; PBS: polarizing beam splitter; FM: flipping mirror; Obj.: 0.25-NA objective lens; PBF: one meter of photonic bandgap fiber; BE: beam expander; SM: galvanometric scanning mirrors; DM: dichroic mirror; PZT: piezoelectric translation stage; MOL: miniature objective lens; F: laser blocking filter; PMT: photomultiplier tube; I→V: current-to-voltage preamplifier; PS: scanning mirror power supply.

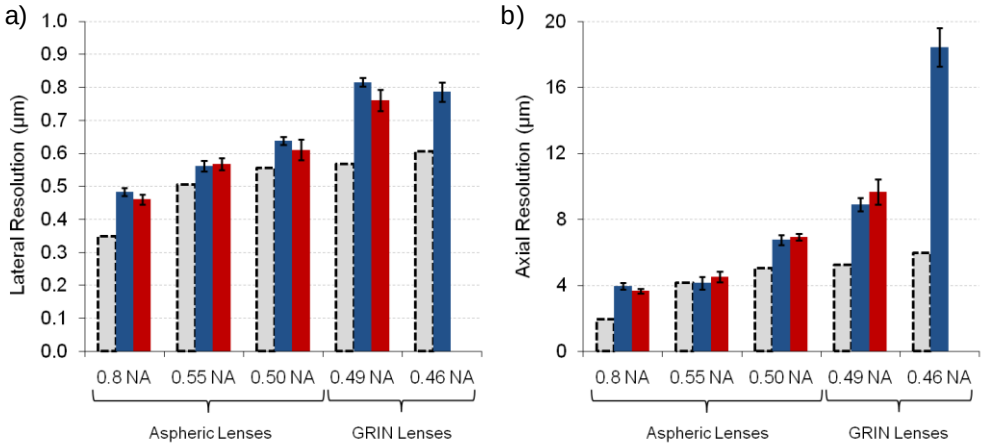

Fig. 3. Lateral (a) and axial (b) resolution measurements for the commercially available miniature lenses summarized in Table 1. The data in blue were measured with the free-space propagated beam. The data in red were measured using a beam collimated by a 0.49 NA GRIN lens after propagation through one meter of PBF. The dashed bars denote the diffraction limit for the specified NA when focusing in media with index of refraction n = 1.34 [12]. Error bars correspond to the standard error of the mean (n = 12).

Figure 3 provides the results of the lateral and axial PSF measurements, with and without fiber delivery. The previously measured PSF of the GRIN lens used in the 18-mm probe is also provided for comparison. From Fig. 3, the effect of fiber delivery and GRIN lens collimation appear to be insignificant. Given the 0.17 NA of the PBF and the 0.49 NA of the GRIN collimating lens, only a small portion of the full NA (and thus a small portion of the

#141745 - $15.00 USD Received 26 Jan 2011; revised 23 Feb 2011; accepted 18 Mar 2011; published 13 May 2011

clear aperture) of the GRIN collimator is used during fiber collimation, which may explain why GRIN lens aberrations do not affect the beam quality during fiber delivery.

During the axial PSF measurements, we measured the PSF in agar and therefore needed to scale the displacement of stage (Δz_{stage}) according to the ratio of the refraction angles at the interface of air to agar to reflect the actual focal shift (Δz_{focus}) in agar. When optical rays pass through media with different indices of refraction, the refracting optical arrays at the interface will cause the focal point to shift according to [14,15]

$$\Delta z_{focus} = \frac{\tan\left(\sin^{-1}\left(NA/n_{air}\right)\right)}{\tan\left(\sin^{-1}\left(NA/n_{agar}\right)\right)} \cdot \Delta z_{stage}, \quad (1)$$

where n_{air} and n_{agar} are the indices of refraction in air and agar, respectively. For instance, the ratio of the tangents is equal to the 1.46 for NA = 0.55. Therefore, the scaling plays a crucial role in accurate calculation of the axial PSF.

When isolated from the rest of the miniaturized optical system and used as the objective lens in a bench-top setup, the influence of spherical aberrations in both the GRIN lenses is immediately apparent. The axial resolution of the 0.46 NA NSG lens is approximately 3 × larger than the diffraction limit. While the 0.49 NA GRINTECH lens shows marked improvement in the axial resolution, it still remains far from the diffraction limit. It should be noted that GRINTECH has recently offered a 0.65 NA compound GRIN lens with improved aberration correction that was not available at the time of testing [13].

Not surprisingly, the highest resolution is achieved using the 0.8 NA aspheric lens. This lens does not exhibit diffraction-limited performance, however, most likely due to the large difference between the imaging wavelength of 753 nm and the lens design wavelength of 1550 nm. On the other hand, the 0.55 NA aspheric lens demonstrates diffraction-limited axial resolution with nearly diffraction-limited lateral resolution in our test system. This lens is a particularly attractive objective lens candidate due its small 2.4 mm diameter and long 0.88 mm working distance. The increased working distance can enable imaging through a cover slip or optical window, which would allow housing of the system inside of an endoscope insertion tube. From these measurements, we can identify both the 0.8 and the 0.55 NA aspheric lenses as potential miniature objective lens candidates.

2.3 Other critical components: PBF and MEMS mirror

In addition to improving the miniature objective lens, the remaining critical components of the probe, namely the air-core PBF and the MEMS scanning mirror, were also improved for use in the revised probe. For laser delivery, a three meter length of air-core PBF was coupled to a compact 1-mm diameter collimating assembly. By increasing the length of PBF from one meter in the 18-mm probe to three meters in the new probe, the dispersion in the fiber is tripled. The increased dispersion allows for greater pre-chirping of the amplified microsurgery laser pulses before their coupling into the fiber. It thus permits the delivery of higher pulse energies without damaging the proximal end of the fiber. Using a three meter PBF we increased the pulse energy out of the PBF by 20% to 1.6 μJ. The collimating assembly utilizes a 0.5-mm diameter GRIN lens designed to produce a collimated beam with 425 μm $1/e^2$ diameter. The compact fiber collimation assembly allows integration into the probe housing while providing a 15% larger beam diameter than in the 18-mm probe.

The new MEMS scanning mirror is based on the same design as the mirror used in the 18-mm probe [16]. In the new device, the mirror area has been increased from 500 μm × 500 μm to 750 μm × 750 μm, while the total size of the MEMS chip is 3.0 mm × 3.2 mm. The mirror surface is bare silicon with a measured reflectivity of 30% for the largely depolarized laser light as delivered from the PBF at near 753 nm wavelength. By driving opposing comb banks

#141745 - $15.00 USD Received 26 Jan 2011; revised 23 Feb 2011; accepted 18 Mar 2011; published 13 May 2011

180° out of phase with a sinusoidally varying voltage signal, we measured resonant optical deflections of ± 7.1° and ± 15.3° at resonant frequencies of 2.26 kHz and 0.98 kHz, using a peak driving voltage of 45 V for the inner and outer axes respectively.

The increase in both collimated beam size and scanning mirror aperture both serve to increase the number of resolvable spots of the new probe, which provides the primary constraint on the imaging performance. The following section explores this constraint and the impact of aberrations on the final optical design of the new probe.

3. Optical system design

The main challenge in the optical design of a smaller probe involves optimizing the achievable imaging parameters, such as resolution and FOV, while minimizing the size of the optics. Analysis of the governing design equations can map the achievable FOV and resolution combinations. While these maps provide initial guidance in optimizing the optical system design parameters, there is a need for a more sophisticated design process using optical design software, such as ZEMAX, to account for, and correct, various sources of aberration.

3.1 Analytical modeling

The maximum number of resolvable spots, *N*, is fixed for the given collimated beam diameter and MEMS scanner aperture and deflection angles. We can estimate *N* by dividing the maximum FOV by the lateral resolution (δ_{xy}). Using the paraxial and thin lens approximations, the maximum FOV is simply

$$\text{FOV} \approx f\theta_{obj} = \frac{f\theta_{mirror}}{M}, \tag{2}$$

where f is the focal length of the objective lens, θ_{obj} and θ_{mirror} are the angles of the beam at the back aperture of the objective lens and from the scanning mirror, respectively, in radians, and M is the magnification of the relay lens system between the scanner and the objective lens. The two-photon lateral and axial (δ_z) resolutions are given by the FWHM of the intensity distribution divided by $\sqrt{2}$. For a truncated Gaussian beam [12], the two-photon lateral and axial resolutions are given by

$$\delta_{xy} \approx \frac{K_1\lambda}{2\sqrt{2}\text{NA}}, \tag{3}$$

and

$$\delta_z \approx \frac{K_2\lambda n}{2\sqrt{2}\text{NA}^2}, \tag{4}$$

where λ is the excitation wavelength, NA is the numerical aperture of the system, and n is the index of refraction of the medium. K_1 and K_2 are correction factors accounting for the diffraction experienced by the beam,

$$K_1 = 1.036 - \frac{0.058}{T} + \frac{0.156}{T^2}, \tag{5}$$

and

$$K_2 = 3.5 + \frac{0.33}{T} - \frac{0.73}{T^2} + \frac{0.52}{T^3}, \tag{6}$$

for $T > 0.4$. Here, T is the truncation ratio at the limiting aperture, D, in the optical system, defined as the ratio of the $1/e^2$ beam diameter to the limiting aperture diameter [12]. Lastly, the paraxial approximation provides NA of the optical system as

#141745 - $15.00 USD Received 26 Jan 2011; revised 23 Feb 2011; accepted 18 Mar 2011; published 13 May 2011

$$\mathrm{NA} \approx \frac{D}{2f}, \tag{7}$$

where D is either the aperture at the objective lens, D_{obj}, or the projection of the mirror aperture, MD_{mirror}, depending on whether the objective lens or the mirror is the limiting aperture, respectively.

To understand the impact of relay lens magnification and objective lens choice in the performance of our probe, we estimated the achievable two-photon resolution as a function of the maximum FOV using Eqs. (2) through (7) when focusing in tissue with an index of refraction of n = 1.34. We performed the calculations for each of the miniature objective lenses, given in Table 1, for magnifications ranging from 1.25 to 4.75. In our design, the MEMS mirror is mounted at 45° to the beam, thus the effective aperture of the mirror is 750 µm × 530 µm. Given the input beam diameter of 425 µm, the truncation ratios along the two axes of the MEMS scanning mirror are 0.80 and 0.57, respectively.

Figure 4 presents the theoretical diffraction-limited design curves of resolution versus maximum attainable FOV corresponding to the two mirror axes. The best resolution for each lens corresponds to a magnification of 4.75 × , where the clear aperture of each objective lens is filled, while the worst resolution for each lens corresponds to the lowest magnification of 1.25 × magnification. The inverse of the slope of the lateral resolution plots indicates the number of resolvable spots, N. The area above each curve represents the allowed design space. We oriented the scanning mirror such that the larger mirror deflection angle (± 15.3°) is along the short effective aperture and the mirror provides the limiting aperture, such that the N for the new probe is 436 × 243.

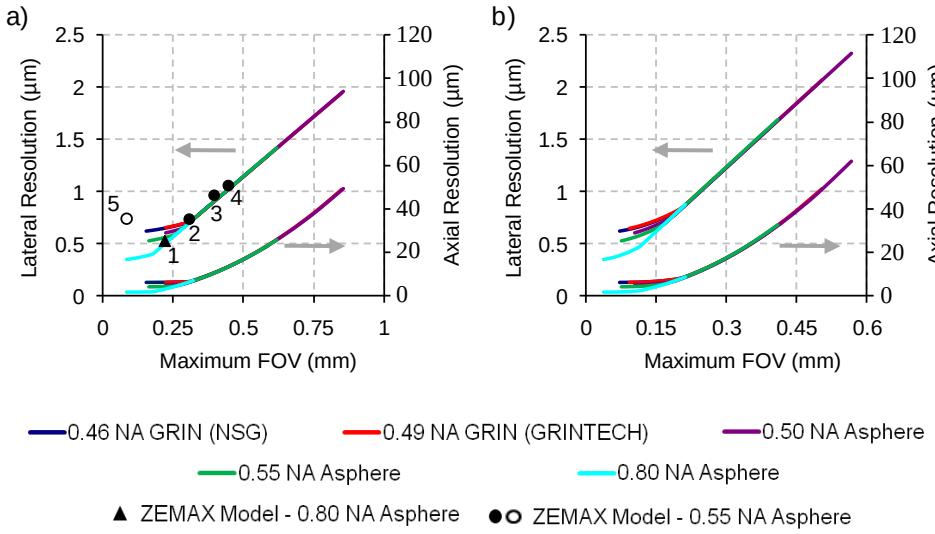

Fig. 4. Calculated diffraction-limited lateral and axial resolutions versus FOV for the specific collimated beam size and the MEMS mirror used in the new probe and the miniature objective lens candidates given in Table 1. The plots correspond to the outer and inner axes of the MEMS mirrors, (a) and (b) respectively. The optical deflection angles and effective apertures of the outer and inner mirror axes are ± 15.3° and ± 7.1°, and 530 µm and 750 µm, respectively. The collimated beam size of 425 µm corresponds to the 0.5-mm GRIN collimation lens used in the probe. Data points represent ZEMAX simulation results, with solid markers indicating optimized custom lenses and the hollow circle indicating a system using commercially available spherical relay lenses (only the diffraction-limited portion of the maximum FOV shown). Magnifications for the models are (1) 1.75 × , (2) 2.38 × , (3) 1.98 × , (4) 1.82 × , and (5) 2.32 × .

In the range of small relay lens magnification (large maximum FOV) that results in underfilling of the back aperture of the selected objective lenses, the MEMS mirror provides

#141745 - $15.00 USD Received 26 Jan 2011; revised 23 Feb 2011; accepted 18 Mar 2011; published 13 May 2011

the limiting aperture, and thus determines the number of resolvable spots. As a result, the design curves for different objective lenses collapse to the same *N* dictated by the mirror. In this range, each objective lens can simultaneously achieve the same maximum FOV and resolution for a suitable magnification from the relay lenses, in the absence of aberrations.

As relay lens magnification increases and thus the beam size at the back aperture of the objective lens increases, the maximum FOV decreases due to demagnification of the scanning angle. Once the relay lens magnification has increased to where the objective lens becomes the limiting aperture, the slope of the plot begins to deviate from the number of resolvable spots dictated by the mirror aperture. Note that the maximum number of resolvable spots decreases once the objective lens becomes the limiting aperture. Thus optimal imaging performance is obtained by filling the mirror more than the objective lens, as is well known [17]. In this high-magnification regime, the objective lens is the limiting aperture. Thus the resolution along each axis is determined by the NA of the lens and is the same for both axes. Conversely, for lower magnifications, where the rectangular effective aperture of the mirror is the diffracting aperture, the analytical model predicts an increasingly elliptical focal spot.

The axial resolution plots in Fig. 4 provide additional guidance for the design because the axial resolution degrades much more rapidly with increasing FOV as the objective lens becomes increasingly under-filled. For instance, a design shift in the lateral resolution from 0.9 µm to 1.5 µm could increase the maximum FOV from 390 µm to 655 µm with little loss in resolvable features owing to the lateral resolution. However, the axial resolution would degrade substantially from 10.4 µm to 29.1 µm, seriously impairing the optical sectioning capabilities of the endoscope.

3.2 ZEMAX numerical modeling of the laser excitation pathway

The analytical model shown in Fig. 4 ignores the impact of aberrations arising from the objective lens or the intermediary relay lenses. From the bench-top testing of the miniature objective lenses, we observe that lens aberrations clearly play an important role. To explore the impact of aberrations, we have constructed a computer-aided model of the 9.6-mm probe design using ZEMAX optical design software.

Figure 5 shows the optical system studied in the ZEMAX model. The system consists of (1) an input beam, (2 and 3) two relay lenses, (4) a right angle prism, (5) a dichroic mirror, (6) an objective lens, and (7) a sample. To model the effects of diffraction from the MEMS scanning mirror, the input laser beam is defined by an entrance pupil diameter of 530 µm, corresponding to the short effective aperture of the MEMS mirror at 45°. We used this model to design the optical system for different design points on the curves shown in Fig. 4a by optimizing the relay lens pair to achieve a target resolution on the curve.

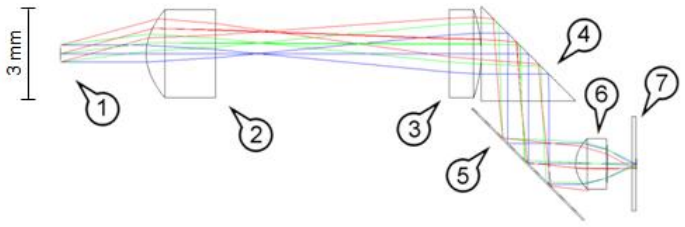

Fig. 5. Optical layout used in ZEMAX modeling of the 9.6-mm probe. The blue, green, and red lines represent the scanned laser beam (1) and correspond to field angles of 0°, 7.1°, and 15.3°, respectively. This model shows a custom-designed relay lens pair (2 & 3) with an effective relay lens magnification of 2.38 × , a right angle prism (4), dichroic mirror (5), and the 0.55 NA aspheric objective lens (6). The sample (7) is modeled as seawater, covered by a glass coverslip.

As a starting point for the design of the relay lens system, we used commercially available aspheric lenses (AC510, Anteryon; and 352550, Lightpath Technologies) with their lens clear apertures increased to 3 mm to improve transmission of larger scan angles. This relay lens

#141745 - $15.00 USD Received 26 Jan 2011; revised 23 Feb 2011; accepted 18 Mar 2011; published 13 May 2011

system provides a nearly diffraction-limited on-axis two-photon resolution. However off-axis aberrations, dominated by astigmatism, quickly degrade the resolution with increasing scan angle. We therefore optimized the lens designs to find the optimal performance of this optical system. To ensure the final lens designs could be easily manufactured, each lens was kept as a plano-convex lens with one aspherical surface. Also, since miniature aspheric lenses are often produced through a molding process, the glass types used in the commercially available lenses (N-BAK and CO550) were used as well.

The prism and the dichroic mirror are modeled from commercially available optics (055-003, OptoSigma, and FF670-SDi01, Semrock, respectively). For the objective lens, the 0.55 NA aspheric lens was initially selected based on its combination of diffraction-limited performance, as shown in the previous section, and long working distance.

The sample was modeled as a microscope cover slip having a thickness of 170 μm (BK7, n = 1.511) with seawater (n = 1.340) as the sample medium, to account for any spherical aberrations arising from tissue or an optical window. The beam is focused at about 30 μm deep under the tissue surface. Since future clinical applications will require focusing into tissue, it will be beneficial to house this probe behind an optical window so that the optical system can be moved axially and/or laterally to adjust the location of treatment.

When optimizing the optical system using commercially-available relay lenses (either spherical or aspherical), it was not feasible to achieve optimized objective lens designs that maintained diffraction-limited focusing over the entire FOV while maintaining surfaces that were practical for manufacturing. Instead, we focused on designing simple relay lenses to work in conjunction with the miniature objective lens candidates explored earlier.

In the ZEMAX model, the radius of curvature, thickness, conic constant, and aspheric constants of each relay lens were established as variables to be optimized, along with the distance between the relay lenses and the distance between the effective MEMS aperture and the first relay lens. The distance between the second relay lens and the objective lens was fixed to the minimum distance of 6 mm dictated by the prism and dichroic mirror. We then constructed the merit function to optimize these variables to reach specified values of diffraction encircled energy (DEE) at each field angle, with each weighted equally. By selecting DEE target values corresponding to different desired spot sizes, the software could be guided to optimize the relay lens pair for different magnifications. In nonlinear optical imaging, a flat FOV is desirable, however not a strict requirement as most of the imaging is meant to occur inside the bulk of the samples. For optimization, we chose to limit the peak-to-valley focal shift, Δ_z, due to the FOV curvature to 10 μm or less.

Table 2. Summary of Modeled Optical System Performance Using Optimized Relay Lens Designs

Objective Lens NA	M	FOV [μm]	δ_{xy} [μm]	N	Δ_z [μm]	St_{min}
0.55	1.82	448 × 212	1.06	423	10	0.86
	1.98	396 × 192	0.962	412	10	0.85
	2.38	308 × 148	0.736	418	5	0.87
	2.32	297 × 142	0.741 – 5.23[1]	N/A[2]	18	0.04
		(85 × 85)[3]	(0.741)	(115)	(5)	(0.80)
0.80	1.75	220 × 104	0.529	416	5	0.90

[1]Where aberrations induce an asymmetric PSF, the encircled energy radius corresponding to half the maximum energy is reported.
[2]N/A: Not applicable due to rapid decrease in *St* across FOV.
[3]The values in parentheses refer to the diffraction-limited portion of the FOV.
(Values in grey correspond to commercially available spherical lens pair.)

#141745 - $15.00 USD Received 26 Jan 2011; revised 23 Feb 2011; accepted 18 Mar 2011; published 13 May 2011

Using this model, we designed three different relay lens systems optimized for use with the 0.55 NA aspheric objective lens with varying magnifications. For each magnification, the minimum Strehl ratio across all design field angles, St_{min}, is maintained above 0.8 for nearly diffraction-limited performance. We performed a similar optimization for the 0.80 NA aspheric objective lens to demonstrate higher resolution while still seeking to maximize *N*.

Table 2 displays a summary of the optimized optical performance for each imaging system. Figure 4a plots these designs against the analytical diffraction-limited model. From Fig. 4a, we see that the analytical model provides an accurate guideline for the optimum imaging performance of the system and that the custom lens designs were able to converge very nearly to this limit imposed by diffraction.

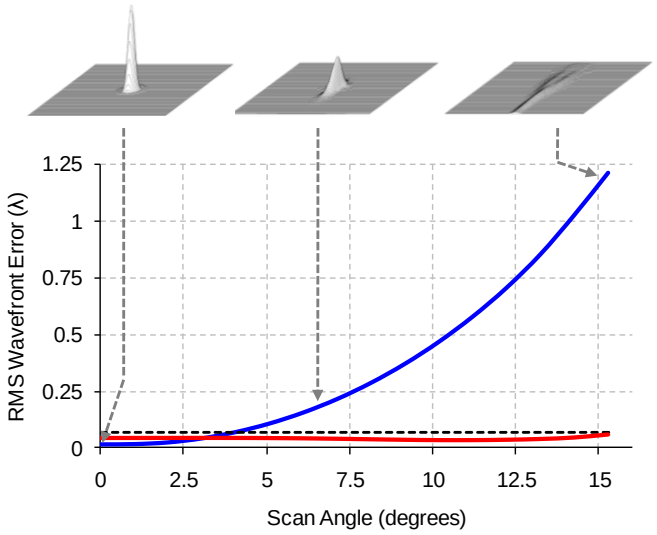

Fig. 6. RMS wavefront error variation with scan angle for the ZEMAX-optimized relay lens pair with 2.38 × magnification (red line) and commercially-available spherical lens pair with 2.32 × magnification (blue line). The calculated PSFs at scan angles of 0°, 7.1°, and 15.3°, are shown above for the commercially-available lens model. The corresponding Strehl ratios are 0.99, 0.36, and 0.04, respectively. The calculated PSFs for the optimized lens pair case at all angles are indistinguishable from the diffraction-limited PSF shown at 0° for the commercial lens pair.

Analyzing the results in Table 2, the use of the 2.38 × magnification lens design with the 0.55 NA aspheric objective lens provides the highest resolution with the longer 0.88 mm working distance. The root-mean-square (RMS) wavefront error variation with scan angle for this system is provided in Fig. 6.

Table 3. Manufacturing Tolerances Sufficient for Maintaining Diffraction-limited Performance

Specification	Tolerance	Units
Radius	0.04	mm
Edge Thickness	0.1	mm
Wedge	60	arc sec
Decenter	0.05	mm
Surface Irregularity	2	fringes

#141745 - $15.00 USD Received 26 Jan 2011; revised 23 Feb 2011; accepted 18 Mar 2011; published 13 May 2011

We assessed the sensitivity of our lens design to manufacturing tolerances and found that most specifications require only "commercial" level manufacturing, with only decenter of the aspheric lens surfaces requiring "precision" manufacturing under conventional definitions [18]. None of the specifications required "high precision" tolerances. Using these tolerances, provided in Table 3, we used ZEMAX to generate 500 randomly perturbed systems and found 98% of the models exhibit maximum RMS wavefront error below 0.069λ, with the worst system only exhibiting wavefront error of 0.077λ. Based on the forgiving tolerance requirements, this lens design should be relatively inexpensive for commercial mass production.

We also examined the sensitivity of the system to alignment and spacing tolerances of the constituent optical components using ZEMAX. For example, by examining the axial separation of the relay lens system, we found that the system remained diffraction limited across all field angles for a tolerance of ± 100 μm, if the focus position at the sample was allowed to shift axially to compensate. Further investigations of the most important alignment and spacing tolerances were completed, but a full discussion of tolerance analysis is outside the scope of this paper.

The results of the relay lens design optimization demonstrate the potential for a fully miniaturized femtosecond laser microsurgery endoscope with robust aberration correction. Using current glass molding technologies, aspheric lenses of this size and complexity can be easily mass-produced for commercial development. For this stage of probe development, however, the production of low quantities of the custom lens designs is not cost effective. Instead, we have chosen to implement commercially available spherical lenses, each with 3 mm outer diameter (NT45-960 and NT48-648, Edmund Optics), to form an inexpensive relay lens pair with a nearly identical magnification of 2.32 × . The ZEMAX model summary of this system is provided in Table 2 and Fig. 6. For this model, the cover slip was removed from sample plane, since this design is not intended for incorporation into a commercial endoscope.

The calculations show that spherical relay lenses can provide diffraction-limited performance at the center of the FOV, with predicted lateral and axial resolutions on-axis of 0.74 μm and 7.4 μm, respectively, inside agar. These values agree with the lateral and axial resolutions predicted by the analytical diffraction model (0.76 μm and 7.5 μm, respectively) to within 5%. The maximal predicted FOV with this design is 297 μm × 142 μm, however off-axis aberrations, dominated now by coma, increase drastically with increasing scanning angles similar to the stock aspheric lenses. Only the central 85 μm maintains St ≥ 0.8 (blue line in Fig. 6). Though aberrated, this design provides an inexpensive means of verifying whether the theoretical performance of the ZEMAX model can be achieved experimentally prior to commissioning expensive custom lenses. Because these lenses possess similar dimensions and focal lengths to the custom lenses, the endoscope housing can be designed around these lenses and potentially reused with the custom lens design at a later date.

3.3 Collection fiber optimization

We built a separate model to analyze the collection pathway, shown in Fig. 7a. This part of the pathway consists of all of the optical elements between the source of the emitted light, located inside the sample, and the PMT detector. Given the 2.4 mm outer diameter of the chosen objective lens, the same 2 mm-diameter collection fiber used in the 18-mm probe is utilized without increasing the final packaged dimensions. A short pass dichroic mirror ($\lambda_{cut\text{-}off}$ = 670 nm; FF670-SDi01, Semrock) was selected to pass the emitted light and was modeled as a perfectly transmitting glass plate with the dichroic mirror's dimensions of 4 × 5 × 1 mm^3. The previous lens (f = 4.0 mm, 0.60 NA; C610TME-A, Thorlabs) directing the light from the fiber into the PMT (H7422-40, Hamamatsu) is reused as well [10]. Specifically, the PMT cathode was modeled using a detector surface the same size as the PMT cathode inside an absorbing housing with the same dimensions as the PMT housing.

To approximate the scattering properties of epithelial tissue for the emitted fluorescence, the sample is modeled as a block of seawater (n = 1.340) with bulk scattering defined by a Henyey-Greenstein phase function using a mean scattering length, l_s, of 29 μm and an

#141745 - $15.00 USD Received 26 Jan 2011; revised 23 Feb 2011; accepted 18 Mar 2011; published 13 May 2011

anisotropy factor, *g*, of 0.75 [19]. Emitted light arising from two-photon fluorescence is modeled by a point source embedded inside the seawater block. The point source is modeled as isotropically emitting 500,000 rays at a wavelength of 475 nm, corresponding with the emission of many intrinsic fluorophores, such as NADH [20]. We varied the depth of the source inside the sample while maintaining a fixed focal length from the objective lens to simulate increased imaging depth.

The collection fiber is modeled by two concentric cylinders with inner and outer indices of refraction of 1.490 and 1.402, to match the total internal reflection properties of the actual fiber. As the model is only intended for comparison of relative collection efficiencies between design changes, rather than an absolute quantitative measurement, attenuation and bending in the collection fiber are ignored. Relative changes in collection efficiency can be determined by comparing the number of rays that reach the PMT cathode in this original model with the number of detected rays after any modifications.

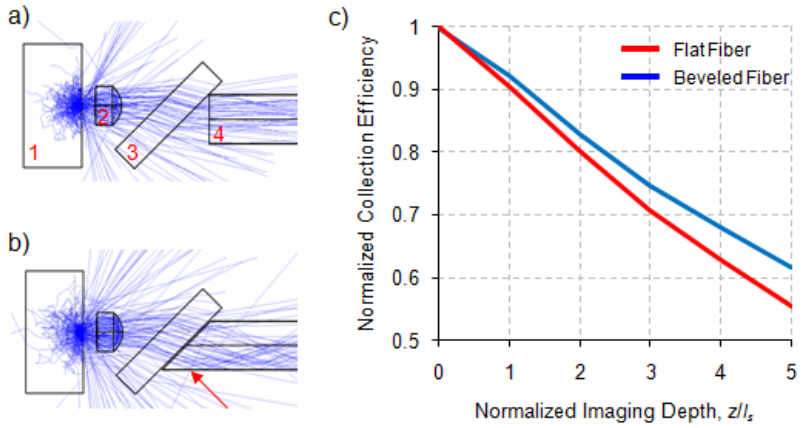

Fig. 7. Addition of a 45° bevel to the collection fiber to improve collection of scattered light. a) The model utilizes (1) a scattering tissue block containing a point source as the sample, (2) the 0.55 NA aspheric objective lens with a long 0.88 mm working distance, (3) the dichroic mirror, and (4) the 2 mm plastic optical collection fiber. b) The addition of a 45° bevel (red arrow) enables the collection fiber to sit flush with the dichroic mirror, enhancing collection of scattered rays. c) The impact of the beveled fiber tip on the number of rays detected from the PMT for varying imaging depths, where depth has been normalized by scattering length, l_s, of 29 µm.

As in 18-mm probe, an air gap exists between the dichroic mirror and the entrance to the collection fiber in which some emitted light may be lost. The air gap is a result of the 45° angle of the plate dichroic mirror (see Fig. 7a). To capture the lost light, we introduced a matching 45° bevel to the distal end of the collection fiber, shown in Fig. 7b, allowing it to sit flush with the dichroic mirror.

Figure 7c displays the number of rays detected by the PMT for both the beveled and flat fiber tips with increasing imaging depth, normalized by the number of rays detected when the focus is at the sample surface. When the focus is modeled to be at the surface of the sample, the emitted light is unscattered and is well collimated by the objective lens. Not surprisingly, this case results in the largest percentage of collected light. As imaging depth increases, more of the emitted light is scattered and accordingly fewer rays enter the objective lens. While both the flat and the beveled fiber tips exhibit decreasing collection efficiency as the imaging depth increases, the beveled fiber tip is less sensitive to increased scattering due to the closer interface between the fiber and the dichroic mirror. By creating a 45° bevel at the distal end of the collection fiber, this model predicts increases in collection efficiency up to 10% over the flat fiber tip at an imaging depth of 5 scattering lengths. This modification should slightly improve the collection efficiency of the 9.6-mm probe for sub-surface tissue imaging.

#141745 - $15.00 USD Received 26 Jan 2011; revised 23 Feb 2011; accepted 18 Mar 2011; published 13 May 2011

4. The 9.6-mm diameter probe

The final optical components of the probe, shown in Fig. 1b, consists of (1) three meters of air-core PBF delivering femtosecond laser pulses to a 0.5-mm diameter GRIN collimating lens with a right angle total internal reflection (TIR) prism affixed. The laser pulses are scanned off (2) a two-axis MEMS scanning mirror, through (3) a spherical lens pair and a 5 mm TIR prism to (4) a 0.55 NA aspheric objective lens. Collected emission light is passed through (5) a 4 × 5 mm^2 short-pass dichroic mirror to a 2-mm core, 0.50 NA collection fiber.

4.1 Probe housing

To package the optical system, we designed a modular housing (Fig. 1c) fabricated by ProJet Ultra High Definition three-dimensional printing. This technique is capable of quickly producing small polymer parts with a typical accuracy of 25 – 50 μm. The modular housing allows individual optics to be aligned in sub-assemblies using passive alignment techniques, while the final system alignment can be achieved actively using a beam profiler and micromanipulators. The final packaged dimensions of the new femtosecond laser microsurgery and microscopy probe are 9.6 mm in diameter and 23 mm in length. These reduced dimensions are nearly 50% smaller in both diameter and rigid length from the first probe, occupying only a 1/5 of the previous probe's volume (Fig. 1a). The probe is small enough to enable use in the oral cavity, in open surgical sites, or through the insertion tube of a commercial colonoscope as a custom endoscope.

4.2 Imaging performance characterization of 9.6-mm diameter probe

To test the imaging performance of the new 9.6-mm probe, we measured the PSF and imaged benchmark microscopy samples, such as pollen grains and rat tail tendon, to compare image quality and combined excitation and collection efficiency. The experimental setup used to demonstrate the probe is shown in Fig. 8. During imaging, the MEMS scanning mirror is resonantly driven on both axes by sinusoidal voltage signals, with driving frequencies of 2,263 Hz and 979 Hz, for the inner and outer axes, respectively. The effective image magnification can be controlled by varying the peak driving voltage. The collected signal from the resulting Lissajous scan is sampled at 4 MHz through a high-speed preamplifier (DHPCA-100, FEMTO Messtechnik) before being reconstructed into 512 × 512 pixel images. The image reconstruction is conducted at a frame rate of 7 Hz, rather than the Lissajous pattern repeat rate of 1 Hz, to gain increased temporal resolution and decrease single-frame laser exposure [21].

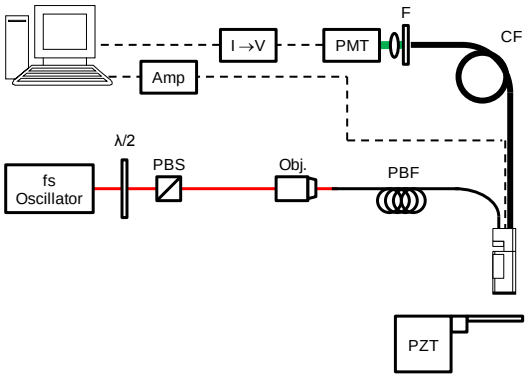

Fig. 8. Experimental setup for testing the 9.6-mm probe mounted above a piezoelectric sample holder. λ/2: half wave plate; PBS: polarizing beam splitter; Obj.: 0.25-NA objective lens; PBF: three meters of photonic bandgap fiber; PZT: piezoelectric translation stage; CF: one meter of plastic optical collection fiber; F: laser blocking filter; PMT: photomultiplier tube; I→V: current-to-voltage preamplifier; Amp: 200 V MEMS driving amplifier.

#141745 - $15.00 USD Received 26 Jan 2011; revised 23 Feb 2011; accepted 18 Mar 2011; published 13 May 2011

We measured the PSF using a bead-in-agar phantom similar to the samples used to characterize the miniature objective lenses in a table top system. We placed a glass coverslip in between the objective immersed in air and the agar phantom. This arrangement might represent better the clinical scenario where there can always be an air gap between the glass-sealed probe and the imaged tissue. In this instance, we used 500 nm fluorescent beads (F-8813, Invitrogen) to improve the signal-to-noise ratio of our measurements. For benchmark samples, we imaged fixed pollen grains (30-4264, Carolina Biological Supply Co.) and rat tail tendon. Rat tail tendon was prepared from a tail harvested from a Sprague Dawley rat, after the animal had been euthanized as required for an unrelated approved research protocol at the Animal Resource Center of The University of Texas at Austin. We also image fresh porcine vocal fold tissue obtained from a local slaughterhouse and stained with a 5 µM solution of the nuclear stain Hoechst 3342. Vocal fold tissue is of particular interest, as vocal fold scarring presents a potential application for image-guided femtosecond laser microsurgery [9].

The FWHM of the Gaussian fits to the lateral and axial PSFs (Fig. 9) are 1.27 µm ± 0.03 µm and 13.5 µm ± 0.54 µm, respectively. The measurements are averaged across 12 beads over a 30 µm FOV and the reported errors correspond to the standard error of the mean. To estimate the exact scale of the focal shift described in Eq. (1), we used ZEMAX modeling of the optical system. Taking into account minor spherical aberrations of the optical system and the underfilled conditions of the objective lens that reduces its effective NA to 0.46, the ratio of the focal shift to mechanical displacement $\left(\Delta z_{focus}/\Delta z_{stage}\right)$ was observed to be 1.36, as opposed to 1.40 predicted by Eq. (1) for NA = 0.46. The mechanical displacement was scaled accordingly using the ZEMAX value, which realistically models the optical system performance. We also took into account the change in the lateral FWHM spot size due to deconvolution of a 500 nm bead which was under 5% and ignored the change in the axial resolution which was below 0.5%.

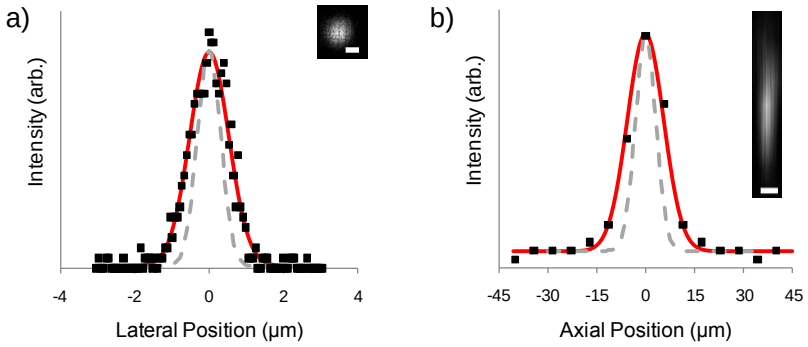

Fig. 9. Example lateral (a) and axial (b) point spread function measurements for the 9.6-mm probe. The raw data from a representative bead is shown in black and the Gaussian fit to the data is provided in red while the diffraction-limited PSF is shown as a dashed gray line. The average FWHM of the lateral and axial PSFs are 1.27 µm and 13.5 µm, respectively. The inset images show *x*-*y* (a) and *x*-*z* (b) plane reconstructions of a single 500 nm bead used for PSF measurement, with 1 µm scale bar. The average power of the laser at the sample was 27 mW.

The measured PSF of 9.6-mm probe represents a notable improvement over the 18-mm probe, with a 23% decrease in lateral spot size and an 18% decrease in axial spot size. The measured PSF is significantly larger than the PSF predicted by the ZEMAX model, however. The model predicted that with a perfect Gaussian beam and ideal alignment the optimum lateral and axial resolutions at the center of the FOV would be 0.74 µm and 7.4 µm, respectively. The departure of the measured resolutions from the predicted values is most likely attributable to spherical aberration arising from filling the back aperture of the 0.50 mm collimating GRIN lens and aberrations arising from slight misalignments during assembly. To avoid these aberrations, future designs should incorporate a collimation assembly design that

#141745 - $15.00 USD Received 26 Jan 2011; revised 23 Feb 2011; accepted 18 Mar 2011; published 13 May 2011

utilizes a larger aperture collimating lens. Because of these aberrations, no statistically significant variation in PSF was measured across a 150 µm FOV, despite the ZEMAX model predicting increasing aberration outside of the central 85 µm. Despite not being diffraction-limited, however, the axial resolution of 13.5 µm is still improved over the 16.4 µm axial resolution of our previous 18-mm probe.

Figure 10 present examples of two-photon fluorescence and second harmonic generation images taken with the 9.6-mm probe. Imaging the pollen grains (Fig. 10a), spikes along the outer shell can be resolved a little better as compared to the previous 18-mm probe. The average laser power used to image the pollen grain was 9.8 mW, which is approximately 3 × less than the power used to image similar pollen in other published miniature two-photon microscopes [22,23]. Similarly, second harmonic generation imaging of rat tail tendon (Fig. 10b) provides visualization of highly aligned collagen fibers using only 20 mW average laser power at the sample, which is 2-3 × less than other similar published systems [24–26]. Even at high magnification, the contrast of the fiber bundles is somewhat low with this probe. This low contrast is likely due to the fiber bundles being smaller than the axial resolution and densely packed together. Still, the density and orientation of the fiber bundles can be resolved from the intrinsic SHG signal, which may prove useful in detecting scar tissue in vocal fold tissue [9].

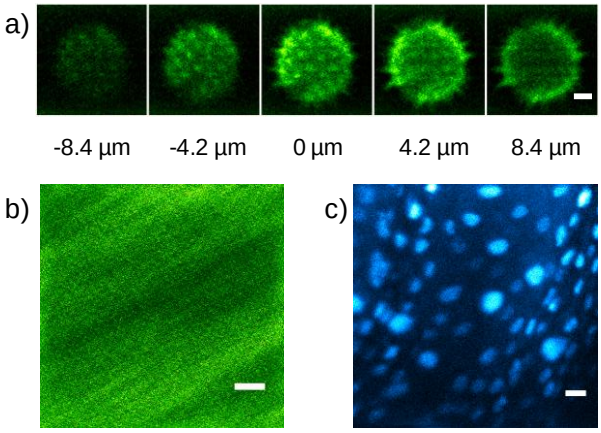

Fig. 10. Representative two-photon fluorescence and second harmonic generation images taken with the 9.6-mm probe. a) A series of images taken at axial locations separated by 4.2 µm through a single pollen grain. The distances from the central focal plane are provided below the images. b) A high-magnification second harmonic generation image of rat tail tendon, showing highly aligned collagen fiber bundles. c) A maximum intensity projection of a ~70 µm thick image stack of freshly excised porcine vocal fold, stained with Hoechst 3342, showing nuclear detail. Average laser power at the sample is 9.8 mW, 20 mW, and 35 mW, for a) – c), respectively. Scale bars are 5 µm in a) and b), and 10 µm in c). All images are 14 frame (2 second) averages.

Lastly, images of fluorescently labeled vocal fold tissue (Fig. 10c) demonstrate that the 9.6-mm probe can provide morphological detail of tissue topology as well as nuclear size and spacing in epithelial tissue, which could be used to guide microsurgery. The average laser power at the sample during imaging of stained vocal fold tissue is 35 mW.

From the above comparison of the imaging powers used on the common microscopy samples, such as pollen and rat tail tendon, the combined excitation and collection efficiency of the new 9.6-mm probe compares favorably with other published fiber-coupled nonlinear imaging probes. This efficient use of imaging power is chiefly due to the large core, large NA collection fiber used to collect the emitted light and its placement close to the objective lens.

These imaging results show different ways of how nonlinear imaging might eventually be used to guide laser microsurgery in a clinical setting. First, the probe can enable visualization of collagen by collecting second harmonic signal that provides a strong signal source as shown in Fig. 10b. We have previously shown that SHG from collagen can be useful in

#141745 - $15.00 USD Received 26 Jan 2011; revised 23 Feb 2011; accepted 18 Mar 2011; published 13 May 2011

navigating vocal fold tissues and collagen is a major constituent of scarred vocal fold [9]. Though individual collagen fascicles are hard to identify using the probe, the density of collagen and the orientation can be determined, which will likely be critical in determining the extent of scarring. Second, the probe can enable imaging of the exogenous contrast agents that can be easily employed to identify structures of interest as shown in Fig. 10c. For applications where the desired surgical target might be difficult to find with a microscopic field of view, the probe can be preceded with a wide-field imaging modality, such as white light or fluorescence. Alternatively, gold nanoparticles can act as bright plasmonic agents for providing imaging contrast [11,27].

5. Conclusions and implications to microsurgery

In summary, we have further refined the optical design of our femtosecond laser microsurgery and nonlinear imaging probe to improve its performance in terms of resolution while integrating all components into a single housing approximately half the size of our original 18-mm probe. Despite the further miniaturization, the imaging resolution of the new probe is improved, with a near 20% decrease in both axial and lateral spot sizes over our previous probe. Analytical and numerical modeling of the optical system show the potential for even further resolution enhancement and larger FOV with two simple custom lenses. Realization of this potential will require improved management of aberration in the fiber collimation and during alignment.

The improved axial and lateral resolutions are critical for reducing the amount of laser energy required for initiating ablation. This aspect is important because of the challenges in the delivery of high peak intensity femtosecond laser pulses through fibers. The improved axial resolution also impacts how well we can identify targets in three-dimensional bulk tissue and how well we can confine the damage within tissue during surgery.

The 9.6-mm encircling diameter of the new device is suitable for a great number of clinical applications requiring surgical precision as well as image guidance. It is small enough to allow the probe to be incorporated into the insertion tube of most commercial colonoscopes to form a custom endoscope or packaged inside a 10 mm tube as a hand-held probe. This size is also suitable for use in a laryngoscope for our current development towards treatment of vocal folds [9]. While the treatment of scarred vocal folds will require a probe design specifically tailored for the larynx and designed to scan larger regions, this 9.6-mm probe demonstrates the suitability of this architecture for achieving microsurgery probes of this size. For some other applications, such as the detection and “cleaning” of tumor margins intra-operatively, the 9.6-mm is also small enough to access an open surgical site or to be brought through the insertion tube of certain commercial endoscopes as a custom probe.

For applications inside the ear, sinuses, or requiring access through the accessory channel of a commercial endoscope, further miniaturization would be necessary. These applications, which require significantly smaller dimensions, will likely require piezoelectric fiber scanning to avoid the spatial constraints of the MEMS scanning mirror. Nonlinear imaging endoscopes based upon two-axis MEMS scanning mirrors have been fabricated with diameters as small as 5 mm using a simple single-fiber layout [28]. However, the air-core fiber used here for microsurgery necessitates the use of a separate collection fiber, limiting the minimum probe diameter with this configuration. With further development, femtosecond laser microsurgical probes such as this can enable physicians to achieve the highest level of surgical precision anywhere inside the body.

Acknowledgments

The authors acknowledge support from the National Science Foundation under grants BES-0548673, CBET-1014953, and Career Award, CBET-0846868, as well as a grant from the Texas Ignition Fund by the University of Texas Board of Regents. Also, the authors would like to thank Prof. Joseph Beaman for fruitful discussion and assistance with housing fabrication and Rick Harrison for valuable discussions. The authors would also like to thank Kazunori Hoshino for wire bonding assistance.

#141745 - $15.00 USD Received 26 Jan 2011; revised 23 Feb 2011; accepted 18 Mar 2011; published 13 May 2011